Quantitative validation of a nonlinear histology-MRI coregistration method using Generalized Q-sampling Imaging in complex human cortical white matter

Mihika Gangolli[a], **Laurena Holleran**[b], **Joong Hee Kim**[b], **Thor D. Stein**[c,d], **Victor Alvarez**[c,d], **Ann C. McKee**[c,d], and **David L. Brody**[a,b,e,*]

[a]Department of Biomedical Engineering, Washington University School of Medicine, St. Louis, MO, USA

[b]Department of Neurology, Washington University School of Medicine, St. Louis, MO, USA

[c]Boston University Alzheimer's Disease and CTE Center, Boston University School of Medicine, Boston, MA, USA

[d]VA Boston Healthcare System, Boston, MA, USA

[e]Hope Center for Neurological Disorders, Washington University School of Medicine, St. Louis, MO, USA

Abstract

Advanced diffusion MRI methods have recently been proposed for detection of pathologies such as traumatic axonal injury and chronic traumatic encephalopathy which commonly affect complex cortical brain regions. However, radiological-pathological correlations in human brain tissue that detail the relationship between the multi-component diffusion signal and underlying pathology are lacking. We present a nonlinear voxel based two dimensional coregistration method that is useful for matching diffusion signals to quantitative metrics of high resolution histological images. When validated in *ex vivo* human cortical tissue at a $250 \times 250 \times 500$ micron spatial resolution, the method proved robust in correlations between generalized q-sampling imaging and histologically based white matter fiber orientations, with r = 0.94 for the primary fiber direction and r = 0.88 for secondary fiber direction in each voxel. Importantly, however, the correlation was substantially worse with reduced spatial resolution or with fiber orientations derived using a diffusion tensor model. Furthermore, we have detailed a quantitative histological metric of white matter fiber integrity termed power coherence capable of distinguishing between architecturally complex but intact white matter from disrupted white matter regions. These methods may allow for more sensitive and specific radiological-pathological correlations of neurodegenerative diseases affecting complex gray and white matter.

*Corresponding author contact: brodyd@neuro.wustl.edu.

Keywords

Diffusion MRI; Generalized Q-sampling Imaging; Radiological-Pathological Correlations; White Matter Injury; Chronic Traumatic Encephalopathy

1. Introduction

Chronic traumatic encephalopathy (CTE) is a progressive neurodegenerative disease that has been increasingly linked to patients who have been exposed to repetitive mild brain trauma in sports or blast related injuries (McKee et al., 2009; McKee et al., 2013). While the initial injuries that trigger CTE are often sustained earlier in life, behavioral symptoms of CTE manifest at later stages, including mood changes, cognitive impairment, and dementia (McKee et al., 2009; McKee et al., 2015; Stern et al., 2013). Neuropathological features of CTE include irregularly distributed hyperphosphorylated tau (p-tau) neurofibrillary tangles and astrocytic tangles prominently distributed in the depths of cortical sulci and around cortical blood vessels (McKee et al., 2016; McKee et al., 2009; McKee et al., 2015; McKee et al., 2013). These features, which increase in quantity and severity through stages I–IV, classify CTE as a tauopathy, can only be definitively detected at the present time by post-mortem examination. In addition to characteristic tau pathology, there is also evidence of axonopathy in CTE (McKee et al., 2015; McKee et al., 2013). There is a concerted effort to develop methods to diagnose CTE and impact related axon injury *in vivo* using blood based or imaging biomarkers (Barrio et al., 2015; Bogoslovsky et al., 2016; Mitsis et al., 2014). One potential imaging modality that is currently under consideration as a means to noninvasively detect axon injury and diagnose CTE *in vivo* is diffusion MRI (Arfanakis et al., 2002; Niogi et al., 2008; Rutgers et al., 2008).

Diffusion MRI is widely used for fiber tracking, brain connectivity, and the diagnosis of neurological diseases, however, the underlying interpretation of diffusion MRI signals is often unknown especially in complex white matter. The diffusion MRI signal is based on the microscopic movement of water in brain tissue (Le Bihan, 1995). Water molecules in fluid such as CSF are free to move in any direction, while diffusion of water in gray matter is hindered by cellular components such as neuronal and glial membranes (Edgar and Griffiths, 2014; Le Bihan, 1995). In simple white matter tracts, the high density of axons restricts water diffusion to the preferential axes of the fiber tracts (Behrens et al., 2014; Le Bihan, 1995; Pierpaoli et al., 2001). This property of water diffusion has opened the door to use diffusion MRI to map and assess the fiber integrity of large brain white matter tracts. Regardless of the algorithm, diffusion MRI based tracking relies on the assumption that water diffusion is least hindered on a path parallel to white matter fiber tracts (Behrens et al., 2014). For example, in the streamline tractography method, local fiber orientation is modeled on a voxel-wise level. The tract is then reconstructed by starting with a seed point and then following local fiber orientation (Behrens et al., 2014). Another strategy which can reduce the error propagations commonly encountered in streamline tractography is to use a probabilistic method (Behrens et al., 2014). Such methods are often more successful when attempting to track white matter fibers where there is a higher degree of uncertainty of the

local directionality of the track, a situation where streamline tractography can fail (Hubbard and Parker, 2014).

Fundamentally, all approaches implementing models such as diffusion tensor imaging (DTI) that use a single tensor estimation inevitably fail when there are multiple fiber populations within a single voxel (Behrens et al., 2014; Hubbard and Parker, 2014; Wiegell et al., 2000). White matter in the healthy human brain is estimated to consist of at least 63% complex fiber populations, defined as crossing, bending, branching or kissing fibers (Jeurissen et al., 2013). Therefore, DTI is inadequate when used to model diffusion in the majority of human brain white matter. For example, Reveley et al. (2015) demonstrated that probabilistic tractography based on DTI data could not be performed in approximately 50% of cortical surface structures, most commonly in sulci and gyri (Reveley et al., 2015) due to the rapidly changing fiber orientation, a finding that they further supported using injected dyes to trace axonal projections. In the context of CTE and impact related axonal injury, the white matter regions most susceptible to injury may be adjacent to cortical sulci (Blumbergs et al., 1994; McKee et al., 2009), though the exact patterns in concussive injury have not yet been fully investigated. These white matter tracts are classified as complex due to the high prevalence of curving U-fibers. Modeling diffusion as an orientation distribution function (ODF) has been proposed as an alternative solution to the multiple fiber populations dilemma, but such models require data collection in more directions, are prone to loss of signal and increased noise due the higher degree of diffusion weighting and require small voxel sizes for precise ODFs (Jones and Cercignani, 2010; Jones et al., 1999). Validation of the fiber directionality central to diffusion tractography has proven successful in radiological-pathological correlations of large relatively simple white matter tracts, but remains under investigated in complex white matter regions (Behrens et al., 2014; Budde and Annese, 2013; Hubbard and Parker, 2014; Kier et al., 2004). Furthermore, the complexity of white matter directionality can confound the interpretation of quantitative diffusion imaging parameters if the issue of directionality is not adequately addressed (Hubbard and Parker, 2014). Specifically, without accurate interpretation of directionality, complex but intact white matter cannot be distinguished from white matter with disrupted microstructural integrity. A radiological pathological correlation approach which accounts for complex white matter architecture would therefore be highly useful when interpreting the sensitivity and specificity of changes in the diffusion MRI signal.

A key component and challenge in performing radiological-pathological correlations lies in the area of coregistration of histology to MRI data. First, coregistration is highly dependent on the placement of fiducials that are clear in both the MRI and histology data. Initial studies typically involved drawing regions of interest based on the anatomical locations of the suspected pathology of interest in corresponding locations for both MRI and histology datasets using a brain atlas or clear anatomical boundaries as reference (Donahue et al., 2016; Herrera et al., 2016; Mac Donald et al., 2007; Weiss et al., 2015). However, in the more general case for arbitrary neuropathological features of interest, such as white matter underlying a specific sulcus, regions of interest that are visually distinguishable based on anatomical landmarks would not provide sufficient specificity. Another option is the use of exogenous fiducial markers that can be injected into the tissue prior to imaging, and used as reference points following sectioning and staining however, this approach is highly

vulnerable to inaccurate injections and subsequent migration of the markers resulting in displacement errors as high as 600 μm (Lazebnik et al., 2003; White et al., 2011; Zemmoura et al., 2014). Strategies to perform automated feature extraction have been successful in cases where the gradient of the histological image has a high degree of correspondence with the structural MRI image (Goubran et al., 2013; Goubran et al., 2015). However, an edge detection based approach often fails when coregistering tissue stained for pathological markers which are only localized to specific regions, such as AT8 for tau tangles in sulcal depths, because of high reliance on similar contrast properties of MRI and histology data (Goubran et al., 2013; Goubran et al., 2015).

Second, the choice of method to warp the histology data to the MRI image can also drastically change the accuracy of registration. Linear transformations such as similarity or affine transforms lead to high registration errors at the curving cortical sulci, due to the sudden change in tissue architecture and potential histological processing differences in the adjacent gray and white matter (Breen et al., 2005a; Breen et al., 2005b; Choe et al., 2011; Goubran et al., 2015). Importantly, registration errors in these areas, the primary locations of CTE related pathology, would create a further loss of sensitivity while performing radiological pathological correlations. A nonlinear approach can provide higher accuracy of registration in cases where a single transformation function does not describe the geometry across all of the tissue, particularly in local changes of tissue architecture (Choe et al., 2011; Dauguet et al., 2007; Goshtasby, 1988; Zagorchev and Goshtasby, 2006). Finally, most automated registration algorithms typically involve downsampling histological data to match MRI data resolution (Wang et al., 2015), or upsampling MRI data to match the high resolution histology (Schilling et al., 2016). Thus, typical coregistration approaches result in a loss of sensitivity in situations where the MRI signal may be affected by changes in the tissue microstructure that are not reflected by measures available in downsampled data, most commonly area fraction of positive staining. Because of the technical challenges listed above, validations of radiological pathological coregistration on a voxel wise level have yet to be performed, resulting in a lack of knowledge of how quantitative histological measures directly reflect corresponding MRI metrics.

In the course of our radiological-pathological investigations of brain tissue from subjects with CTE (Gangolli et al., 2015; Holleran et al., 2015) we have recently developed a method to coregister histology and MRI data at a voxel-by-voxel level so that correlations can be performed between high spatial resolution diffusion MRI and quantitative histological data. We validated the method using a variety of measures, most notably an initial radiological pathological correlation of fiber directionality in complex white matter regions. The registration workflow is not restricted to high contrast stains, thus providing a means of assessing subtle morphological changes in histology, and can be applied to perform highly sensitive and specific radiological pathological correlations in CTE and potentially other applications to extract ground truth relationships between the MRI signal and underlying tissue pathology.

2. Methods

2.1 Diffusion MRI Acquisition

Ex vivo human brain tissue blocks of superior frontal cortex (Brodmann Area 8/9), approximately $1 \times 2 \times 3$ cm, with a confirmed neuropathological diagnosis of Stage III or IV CTE (ACM, TDS, VEA) were obtained through the VA-BU-CLF brain bank. All brain tissue samples were stored in periodate-lysine-paraformaldehyde (PLP) fixative, but then refixed in 10% neutral buffered formalin and refrigerated for one week (Fig. 1). Meninges and blood vessels were trimmed from the cortical surface to remove potential artifacts in the MRI data acquisition, such as blood iron and air bubble induced artifacts. Image artifacts were examined using the T2* images. Tissue blocks were rehydrated in 1x phosphate buffer solution (1x PBS) with 0.01% NaN_3 for two weeks prior to MRI data acquisition and stored at 4°Celsius, changing the solution every three days to assure equilibrated rehydration. This rehydration time was determined empirically by finding the time during rehydration at which the T2 relaxation time reached steady state (Supplementary Figure 1). The volume ratio of tissue and 1xPBS was 1:40.

Diffusion MRI data were acquired using an 11.74 T MRI scanner with 120 G/cm gradient (Agilent, Palo Alto, CA), using a two dimensional standard spin echo sequence, which was optimized to produce high spatial resolution data with an in plane resolution of 250 μm × 250 μm and slice thickness of 500 μm. An in-house built cylindrical radio frequency (RF) coil with 2.60 cm diameter and 4.0 cm length was used to obtain diffusion MR data (Supplementary Figure 2). The main axis of the RF coil (resonant) was parallel to the longest axis of each tissue block to improve B1 field inhomogeneity. While a long repetition time (TR) is typically preferred to collect MRI data with high SNR, this also results in longer scan times and therefore requires optimization of the TR time. To address this concern, MRI data of the same tissue section was collected at multiple TR times and the optimal TR time was found to be greater than one second (Supplementary Figure 3). To minimize artifactual MR signal (Miller et al., 2011; Thelwall et al., 2006), tissue blocks were stored in a proton free solution (Fluorinert) prior to scanning (Supplementary Figure 4A). The tissue samples were stored at room temperature twenty-four hours prior to scanning to reduce temperature related diffusion artifacts (D'Arceuil et al., 2007; Kim et al., 2007; Thelwall et al., 2006). Furthermore, multiple slice collection requires multiple RF pulse excitations, which can heat the tissue resulting in increases in diffusivity (Supplementary Figure 4B). Therefore, each MRI data acquisition consisted of 13 slices irrespective of the tissue block thickness to maintain consistent temperature throughout the study. Approximately seven MRI slices per tissue of the collected data were used for analysis to ensure minimal artifacts caused by partial voluming near the top and bottom of the often irregularly shaped tissues.

With these parameters, both DTI (Jones et al., 1999) and Generalized Q-Sampling Imaging (GQI) (Yeh et al., 2010) data were collected. DTI data were acquired using 30 diffusion sensitized gradients (Supplementary Table 1), a b value of 4,000 s/mm^2, four non-diffusion weighted images (b = 0 s/mm^2) and TR/TE = 1400/30 ms with a total scan time of 1.5 hours. Fixed *ex vivo* tissue has reduced water diffusivity compared to *in vivo* tissue, thus requiring

higher b values to compensate for the reduced diffusivity (D'Arceuil et al., 2007; Thelwall et al., 2006). GQI data were acquired using 202 diffusion sensitized gradients (Supplementary Table 2), a maximum b value of 8,000 s/mm^2, ten non-diffusion weighted images (b = 0 s/mm^2) and TR/TE = 1400/30 ms, resulting in a total scan time of 11 hours. The data was filtered using a standard periodic Hamming window to filter any Gibbs ringing artifact (Supplementary Figure 5) of size 160-point × 128-point to match the readout encoding and phase encoding directions. DTI data were reconstructed using the BrainSuitev16a1 diffusion pipeline (Shattuck and Leahy, 2002) to generate eigenvalue and eigenvector files. GQI data were reconstructed in DSI studio (http://dsi-studio.labsolver.org/) using a diffusion sampling length ratio (L) of 0.70, a 4-fold tessellated icosahedron resulting in 162 sampling directions, a maximum of three resolved fibers per voxel, and a balanced full sphere scheme. The orientation distribution function (ODF) calculation was weighted by the square of the diffusion displacement. These parameters were chosen empirically in order to maximize the sharpness of calculated ODFs, which were then exported into MATLAB (Mathworks 2014a) for remaining analysis. As an additional comparison, the DTI data were also reconstructed in DSI studio based on the higher angular resolution data.

2.2 Histology

Following diffusion MRI data acquisition, tissue blocks were refixed in 4% paraformaldehyde, incubated for a minimum of three days in 30% sucrose solution, sectioned into sequential 50 μm sections on a freezing sliding microtome and stored in individual wells to preserve slice location. The tissue blocks were placed on the platform in the same orientation as the acquired MRI images, with the MRI image planning used as a reference to slicing plane and orientation. Every sixth section (250 μm interslice interval) was stained using the Myelin Black Gold II stain for myelinated fibers (Millipore, Billerica, MA), resulting in two Black Gold II sections for each MRI slice. Free floating sections were incubated in six well plates (Corning) filled with Black Gold II solution (Black Gold II powder, resuspended in 0.9% saline solution) pre-heated to 60°Celsius and monitored until they had reached the optimum amount of staining, approximately eight minutes, which was determined by assessing whether fibers could be readily distinguished at x5 magnification (Supplementary Figure 6). To maintain uniform quality of staining across tissue sections, fresh Black Gold II solution was used for each section. Sections were washed with MilliQ water for two minutes and then incubated in 1% sodium thiosulfate pre-heated to 60°Celsius for three minutes to remove excess staining. After three washes in 1xTBS, stained sections were mounted on Superfrost-Plus microscope slides (Fisher, Houston, TX) in an orientation matching that of the corresponding MRI slices and allowed to dry at room temperature overnight. The mounted sections were dehydrated in a series of graded ethanol solutions (50%–70%–95%–95%–100% for two minutes each), and then incubated in two treatments of Xylene for three minutes each. Slides were coverslipped with Cytoseal 60 (Richard Allan Scientific, Kalamazoo, MI), and digital images of the slides were acquired with a Hamamatsu NanoZoomer 2.0 HT System (Hamamatsu) with an x20 objective and stored in an NDPI file format.

2.3 Co-Registration of Histology to MRI

Due to the large files sizes of the originally acquired x20 magnification images, where the linear dimension of the image pixels was 0.52 μm, the NDPI images of the stained sections were downsampled in ImageJ (NIH, Bethesda, MD) using the NDPI tools plugin (Deroulers et al., 2013) to x5 magnification. This magnification preserved morphological details for quantification where the linear dimension of image pixels was 1.84 microns, and the smaller file size allowed for more efficient registration and quantification. Because this downsampled image was still at a higher resolution than the MRI image, co-registration was then performed to warp the histological data to the MRI space. A minimum of 55 anatomical landmarks were manually placed on the x5 image of the Myelin Black Gold II stained section and the same landmarks were placed on the corresponding non-diffusion weighted (b = 0 s/mm^2) diffusion MRI slice which had T2 contrast characteristics. Landmarks were placed at readily identifiable locations along the tissue edges, border between gray and white matter, and at matching features in both gray and white matter. A forward nonlinear moving least squares transformation (Goshtasby, 1988) was applied to transform the MBGII section to the MRI data. An inverse transform was then applied to transform each MRI voxel of the histological data, resulting in a warped grid of regions of interest (each region of interest corresponding to one MRI voxel) that was used to quantify the higher resolution x5 histological image in ImageJ (Fig. 2). Both forward and inverse transforms were performed using a custom script (Supplementary File 1) written in Matlab.

2.4 Validation of Registration

Following co-registration, and generation of voxel-based grids, the accuracy of registration was validated using tools in ImageJ. First, the agreement between MRI and histology to classify voxels into tissue categories was evaluated. To classify Black Gold II registered voxels, a histologically derived trinary white matter mask was generated (Fig. 3). Each Black Gold II image was converted to a 32 bit (grayscale) image, manually thresholded based on staining intensity and blurred using a Gaussian filter with a radius that matched the in plane resolution of the MRI data (250 μm). The coregistered grid obtained from the inverse transformation was then overlaid onto the white matter mask, and the mean intensity within each voxel-based ROI was measured. ROIs with a mean intensity of zero were classified as gray matter, while voxels with a mean intensity of one were classified as white matter. Finally, voxels with a mean intensity that was between zero and one reflected the partial voluming of white and gray matter and were classified as boundary voxels. The gradient of the non-diffusion weighted (b = 0 s/mm^2) MRI image was used to classify MRI voxels into the same three categories. To compare the efficacy of a nonlinear approach to linear transformations which have typically been applied in previous radiological-pathological correlation studies (Choe et al., 2011; Wang et al., 2015), voxel-based grids were generated using an affine transformation included in Matlab. The kappa coefficients of the grids resulting from nonlinear moving least squares vs affine transformations were then compared to determine whether our registration approach provides superior sensitivity when parceling tissue into gray, white, and gray/white matter boundary regions.

Because the registration algorithm relies on user defined landmarks, we carefully tested the susceptibility of nonlinear registration to variability when presented with landmarks with

small shifts of their in plane locations. Intra-user and inter-user reliability was tested by comparing the shift of each registered voxel between two pairs of grids generated by landmarks placed by the same user at two different time points (five days apart). Inter-user reliability was tested by performing the same procedure for landmarks placed by two different users. The shift was calculated as the Euclidean distance between the centroid of corresponding voxels from the first and second grid. A computer simulation was additionally used to test the effects of shifting landmarks between 0 to 1000 μm along both the x and y direction. Random numbers were selected from a uniform distribution and applied to a baseline set of landmarks in Matlab. The total number of registered voxels from the resulting registrations that had not shifted more than the in plane MRI voxel resolution (250 μm isotropic) was then calculated for each interval.

The final validation was a test of the registration method to perform a radiological pathological correlation for a parameter where the relationship between histology and diffusion measure is expected to be very strong. This parameter of interest was fiber directionality, which can be calculated from both the histological data and the diffusion data. Fiber directionality of each ROI corresponding to each white matter voxel was derived from the Myelin Black Gold II data using a custom written macro (Supplementary File 2) in ImageJ (NIH, Bethesda, MD). Each voxel was zero mean normalized and multiplied with a Tukey window ($\alpha = 0.5$) to reduce background and Gibbs ringing artifacts (Fig. 4). A two dimensional discrete Fourier transformation was then applied to each voxel-corresponding ROI to calculate the associated power spectrum, which contains information about fiber directionality and the degree of fiber coherency within an equivalent voxel (Appendix I). Fiber directionality and coherency were extracted by fitting two ellipses to the power spectrum, where each ellipse represented a fiber population. The angle of the preferential axis of each ellipse relative to the main axis of each registered histological voxel was used as the primary orientation of fibers within each voxel. The degree of coherency of each fiber population was calculated as the ratio of the radial (minor axis) to preferential axes to obtain a measure between zero and one, where a higher coherency measure (closer to one) was thought to represent high fiber integrity. For example, a power coherency of 0.17 indicates two fitted ellipses, where the major and minor axes of both ellipses are relatively equal in length, making the ellipses nearly circular. Conversely, a power coherency of 0.81 indicates two ellipses that both have minor axes which are much smaller than their respective major axes. In parallel, the diffusion based fiber directionality was extracted in Matlab from the generalized q-sampling imaging (GQI) data based on the orientation distribution function (ODF) of each MRI voxel. The ODF was stored as a series of three dimensional directional vectors of size $3 \times N$, where N is the number of fiber directions at a subvoxel level, here defined as two. After obtaining the directional vectors of the primary and secondary major fiber components, the orientation angles, θ_n, along the xy plane were calculated using

$$a \cdot b_n = |a||b_n|\sin\theta_n \quad \text{(Eq. 1)}$$

$$\theta_n = \sin^{-1} \frac{a \cdot b_n}{|a||b_n|} \quad \text{(Eq. 2)}$$

where a is the equation of the xy plane (0,0,1) and b_n is the directional vector of either the primary ($n = 1$) or secondary ($n = 2$) orientation. White matter voxels were classified as simple ($n = 1$) or complex ($n = 1$) for all analysis. Furthermore, because the two-dimensional Fourier transformation can only be used to quantify fibers that are in the histological plane, all analysis was restricted to only include voxels where the primary and secondary major fiber components were either fully in plane or made an angle with the z-axis that was less than 45°.

To test the effects of lower in plane voxel resolution on the histological measure of voxel based power coherency, the open source software MIPAV (NIH, Bethesda, Maryland) was used to downsample the raw diffusion data voxels to 500 μm and 1000 μm isotropic resolution. In accordance with the methods described in section 2.3 landmarks were placed on the x5 histology image and the associated slice of the downsampled unweighted (b = 0 s/mm^2) diffusion dataset to generate voxel based grids corresponding to these lower resolutions. A region of interest starting at the gray/white matter boundary and extending 2 mm into adjacent white matter of a sulcus with known fiber disruption was assessed for power coherence on a voxel wise basis using grids with isotropic in plane resolutions of 250 μm, 500 μm, and 1000 μm. ODFs were reconstructed in DSI studio with the parameters described in Section 2.1for the downsampled diffusion data. A two tensor fit was applied on a voxel wise basis to each corresponding Black Gold II sections to calculate fiber orientation. A correlation between GQI based and Black Gold II based fiber orientation was performed, only on white matter voxels that did not have a z-axis angle greater than 45°.

Similarly, the effects of implementing a DTI model with both coarse angular resolution and high angular resolution matching that of the GQI data were tested. DTI based fiber orientation was calculated on a voxel-wise basis. The eigenvector corresponding the largest eigenvalue for each calculated tensor was used as the measure of fiber orientation of each MRI voxel. The orientation angle θ was calculated using

$$a \cdot b = |a||b| \sin\theta \quad \text{(Eq. 3)}$$

$$\theta = \sin^{-1} \frac{a \cdot b}{|a||b|} \quad \text{(Eq. 4)}$$

where a is the equation of the xy plane (0,0,1) and b is the eigenvector corresponding to the largest eigenvalue of the diffusion tensor. The same landmarks used to coregister GQI data to Black Gold II data were used to coregister the DTI data.

To test that power coherence is indeed a measure of white matter disruption, a 2 mm controlled cortical impact (CCI) injury was applied to a male mouse, as previously described (Brody et al., 2007). This level of injury is known to result in thinning of hippocampal and cortical layers, along with positive staining for amyloid precursor protein (APP) and other markers of axonal injury in the acute phase following injury. Twenty-four hours after injury, the mouse was transaortically perfused and the brain was surgically removed from the skull and fixed in 4% paraformaldefyde (PFA) in 1x PBS overnight. The whole brain was then incubated in 30% sucrose for three days, sectioned on a freezing sliding microtome into 50 μm thick sections, and stained for myelinated white matter using Myelin Black Gold II.

2.4 Statistical Analysis

All statistical analysis was performed in Statistica 13.1 (Statsoft Inc., Tulsa, OK). A one-tailed Spearman's correlation coefficient was calculated to measure the correlation between GQI based and Black Gold II based primary and secondary fiber orientations. A one-tailed F-test was used to determine whether there was a significant reduction in power coherence variation across samples when comparing voxels with isotropic in plane resolutions of 250 μm vs 500 μm and 250 μm vs 1000 μm.

3. Results

3.1 Agreement between MRI and histology based tissue classification

A total of 113 MyelinBlack Gold II stained sections from ten tissue blocks were registered to their corresponding MRI slices. Every registered voxel was classified as gray matter, white matter, or gray/white matter boundary, and a Cohen's kappa coefficient was calculated for each registered section to determine the agreement between MRI based and Myelin Black Gold II based voxel classification. Nonlinear transformations resulted in higher kappa coefficients compared with affine transformations (Table 1), measured by calculating the mean kappa coefficient across sections for each tissue block. The difference in registration methods could also be qualitatively observed, in particular at sulci and gray/white matter boundaries (Fig. 5). A linear affine transformation applied the same transformation to each registered voxel, whereas our nonlinear method better compensates for tissue warping and shrinkage that is not uniform across heterogeneous tissue regions. Notably, nonlinear registration results in a high classification agreement of boundary voxels. This indicates that a nonlinear registration method is more reliable than a linear (affine) method when coregistering tissue sections in regions characterized by abrupt in-plane changes in tissue architecture.

3.2 Robustness of landmark placement-based registration

Two sets of registered grids were generated for a subset of registered Myelin Black Gold II sections for each of the ten human *ex vivo* cortical tissue blocks. The nonlinear registration algorithm remained consistent between the two sets of landmarks, so any variability of the grids and registration would be due to a change in the in plane position of the manually placed landmarks. The Euclidian distance was used as a metric of voxel-wise shift and reliability of registration was determined by plotting the cumulative histogram of the shift of all voxels (Fig. 6A–B). Because the MRI in plane resolution was 250 μm × 250 μm, the

percentage of voxels that had shifted less than 250 μm was used as a metric of inter and intra-rater reliability of landmark placement. To maintain registration quality control, a minimum intra-user and inter-user reliability was set to 90%. All investigators placing landmarks showed inter and intra-reliability of landmark placement that was above this threshold.

An additional simulation was performed on established sets of landmarks to determine the robustness of registration, or the tendency of voxels to shift due to increasing changes in landmark placement (Fig. 6C). Landmarks placed on Myelin Black Gold II were shifted along both the x and y axis by drawing random numbers from a uniform distribution where the interval of the distribution reflected the maximum amount of shift. For each distribution and maximum landmark shift, the percentage of registered ROIs equivalent to MRI voxels that had shifted more than 250 μm was calculated and plotted as a function of the distribution interval. As expected, larger amounts of shift in landmarks decreased the percentage of registered ROIs that were below this threshold. However, landmark shifts below 350 μm did not cause the percentage of registered ROIs to fall below 80%. These results indicated a high degree of reliability for our manual landmark-based coregistration method.

3.3 Correlation of diffusion derived and histologically derived fiber orientations

The strength of the relationship between diffusion based and histologically based primary and secondary fiber orientations was used to determine the accuracy of histology to MRI co-registration. Fiber orientations derived from the Myelin Black Gold II data were compared on a voxel wise basis with fiber orientations of corresponding voxels derived from the diffusion data. Because the GQI data had higher angular resolution compared to DTI data, GQI data were the basis for comparison. Strong edges in gray/white matter boundary regions could not be removed by zero mean normalization or windowing, consequently, only registered regions of interest classified as white matter were included in analysis. = When plotting the Myelin Black Gold II based fiber orientations as a function of the corresponding GQI based fiber orientations (Fig. 7), there was nearly a one to one linear relationship between both primary ($p < 0.0001$, $r = 0.94$) and secondary ($p<0.0001$, $r = 0.88$) fiber populations. The agreement between primary fiber directionality was then compared utilizing an affine transformation (Fig. 8). The spread of Black Gold II based fiber orientations for each GQI fiber orientation bin was much broader when comparing primary fiber orientation, but the affine still provided reasonable agreement ($p < 0.0001$, $r^2 = 0.87$). When comparing the correlations of affine vs nonlinear transformations using a difference test, there was a significant difference between the two correlation coefficients ($p = 0.0026$). The results of the linear regression showed that there was a bias in the nonlinear transformation ($y = 1.0x + 10.47$), compared to the affine transformation ($y = 1.0x + 1.952$). Fiber orientation correlations based on nonlinear coregistration had small variance and moderate bias, while correlations based on the affine transformation had larger variance and smaller bias. However, while addition of more sample voxels would reduce the variance of fiber orientation correlation, this would be less applicable when performing correlations in human tissue, where each sample only has a finite number of voxels.

3.4 Limitations of spatial and angular resolution on radiological-pathological correlations

To assess the effects of spatial resolution on the correlation between diffusion derived and histologically derived fiber orientation, Black Gold II stained sections were registered to corresponding GQI diffusion data that was downsampled to either 500μm or 1000 μm isotropic resolution. At these spatial resolutions, the relationship between GQI based and Black Gold II based primary fiber orientations using the two tensor fit resulted in limitations when calculating histologically based fiber orientation (Fig. 9), particularly at 1000 μm isotropic resolution with a low correlation (r = 0.35).

The importance of angular resolution was tested by coregistering Black Gold II stained sections to corresponding DTI data using the original MRI spatial resolution (250 μm in plane). The DTI based fiber orientations were calculated on a voxel-wise basis and compared with fiber orientations derived from corresponding histological data. The tissue block used for this analysis was composed of 4.40% simple white matter and 22.6% complex white matter only with in plane fiber components. 12.11% of the voxels in the tissue block were classified as having one or more major 3D fiber components, and the remaining 60.89% voxels were classified as gray matter. Assessments of the relationship between fiber orientation derived from a low angular resolution diffusion tensor model (30 directions) resulted in low correlations in both simple (r=0.41) and complex (r=0.53) white matter (Fig. 10A–B). Similarly, correlations of DTI based and Black Gold II based fiber orientations resulted in low correlations in both simple (r=0.42) and complex (r=0.54) white matter (Fig. 10C–D) when implementing DTI reconstruction using diffusion data with an angular resolution matching that of the GQI data.

3.5 Assessment of fiber integrity using power coherence

To demonstrate the potential utility of the fully coregistered approach, the power spectrum calculated from the voxel-wise two dimensional Fourier transformation was also used to assess the degree of fiber organization, and whether fiber disorganization could be quantitatively distinguished from crossing fibers. The measure of power coherency was calculated for each voxel classified as white matter based on Myelin Black Gold II staining. Power coherency was calibrated to remain between 0 and 1, where a higher power coherency reflects increased fiber organization. Conversely, decreased power coherency reflects decreased directionality within a registered ROI, and therefore decreased fiber organization. In voxels where fiber components were either fully in plane or had a primary z axis component of less than 45°, we were able to readily distinguish regions of simple, crossing, and disrupted fibers when analyzing white matter adjacent to cortical sulcal depths (Fig. 11). Voxels with simple and crossing fibers had power spectra that spread across narrow ranges of spatial frequencies, reflecting intact fiber integrity with strong directional components. Voxels with disrupted fibers had power spectra that spread across a broad range of spatial frequencies, reflecting reduced fiber integrity with fibers distributed in random orientations.

Because the human tissue used for this study had known CTE pathology with prior history of concussive injury, we also tested whether power coherence would be able to distinguish between uninjured white matter and a positive control of axon injury. This was performed in

a mouse model using a 2 mm controlled cortical impact (CCI) injury as previously described by Brody et al. (2007) (Brody et al., 2007). White matter in the corpus callosum ipsilateral to the injury site showed reduced power coherence compared to the corresponding region of interest in an uninjured animal (Fig. 12).

To test whether spatial resolution limits the ability to measure power coherence in complex human white matter, Black Gold II stained sections were registered to corresponding diffusion data that was downsampled to either 500 μm or 1000 μm isotropic resolution. Power coherence was calculated in regions of interest defined as extending 2 mm into white matter adjacent to sulcal gray matter. At 250 μm, the heterogeneity of these white matter regions was apparent by the large variance of the voxel wise measures of power coherence (Fig. 13). However, as spatial resolution was decreased, both to 500 μm and 1000 μm, there was an observed reduction in the amount of variance of voxel based power coherence, while the mean power coherence did not change. A one-tailed F-test to assess a decrease in variance resulted in significance both when comparing a decrease from 250 μm to 500 μm ($F(1185,395) = 5.43$, $p < 0.001$) and 250 μm to 1000 μm ($F(1185,79) = 1.53$, $p < 0.001$).

4. Discussion

In summary, we have developed a histology to MRI image coregistration workflow that can be applied to explore the neuropathological features that drive MRI signal changes in the brain. This method is not limited to diffusion MRI, and could be applied to various other imaging modalities, provided that there is a corresponding structural image dataset for the basis of registration. Registration results in voxel-based grids that are highly robust due to shifting landmarks, highly sensitive when parceling tissue types, and show strong accuracy when correlating histologically derived measures with MRI parameters. Furthermore, our registration provides an efficient approach to perform arbitrary region of interest based analysis, with manually drawn regions from histology automatically referenced to corresponding MRI voxels.

In this study, the agreement between histological and diffusion based fiber orientations was used throughout as the primary means of validating coregistration accuracy on a voxel wise basis. Prior comparisons of directionality have been performed both in human and mouse tissue, calculating histologically based fiber direction using a Fourier transformation or gradient based approach (Budde and Annese, 2013; Budde and Frank, 2012; Budde et al., 2011; Nazaran et al., 2016), and validating DTI based tractography at high resolutions. At similar spatial resolution, we found that the fiber orientation derived from DTI tensors did not reflect underlying fiber architecture, particularly in complex white matter regions, at both coarse and high angular resolutions. This finding indicates that alternative local reconstruction methods that do not rely on a single tensor assumption are necessary to accurately perform tractography. Because our intent is to perform correlations primarily in cortical tissue which has a complex fiber architecture, we turned to more advanced diffusion methods which could still produce measures of fiber orientation. GQI based ODF peaks were used here as this metric because in white matter, each ODF is been directly calculated based on water displacement (Yeh et al., 2010) compared to alternative q-space methods such as diffusion spectrum imaging, which often requires additional filtering to counter

cutoff effects in the frequency domain (Hagmann et al., 2006). The GQI reconstruction method is therefore able to compensate for rapid changes in fiber orientation in complex white matter between voxels. Consequently, correlations proved to be most robust when comparing fiber orientations calculated using the GQI reconstruction method. Fundamentally, these correlational studies would not have been successful without careful optimization of the method parameters, such as spatial resolution and choice of histology-MRI transformation.

A primary advantage of our coregistration approach is that histological parameters for correlation can be based on high resolution digital image of histology, so analysis is not limited to area fraction of positive staining. For example, in this study, we compared fiber orientation on a voxel-wise basis in both simple and complex white matter regions to validate the registration technique, which would not have been possible in downsampled histological data that is compressed to match MRI resolution. When applied to analysis of additional histological markers, such as immunostaining for hyperphosphorylated tau, injured axons, and activated astrocytes or microglia, we can explore morphological features of neuropathological markers, such as circularity, and randomness of cells within regions of interest that correspond to voxels in MRI space. This may provide increased specificity in radiological-pathological correlations for both gray and white matter pathology which contain multiple cellular components that may contribute to the diffusion MRI signal (Edgar and Griffiths, 2014; Le Bihan, 1995).

Our derived measure of power coherence also reflects an advantage of high resolution histological analysis. When exploring axon injury at acute time points, markers such as Myelin Basic Protein (MBP) and β-APP have been successful (Blumbergs et al., 1989; Blumbergs et al., 1994; Johnson et al., 2013; Ryu et al., 2014) while chronic white matter demyelination has been used as a metric of injury in severe cases of traumatic brain injury (Strich, 1956), and multiple sclerosis (Wang et al., 2015). For both cases, the primary quantitative metric is area fraction of positive staining. In the CTE cases that we have examined, there was no detectable staining for markers such as β-APP or compacted neurofilament (not shown); such staining may not be detectable in the chronic phase of injury which is years after the initial insults to tissue (McKee et al., 2009; Stern et al., 2013). Similarly, Bennett et al. (2012) determined that β-APP was unable to distinguish between uninjured and injured mice in a mouse model of repetitive concussive injury, suggesting a different mechanism of axonal injury (Bennett et al., 2012). Stains such as Black Gold II for myelin do show demyelination, again in severe cases of white matter injury (Savaskan et al., 2009). As an alternative to demyelination and decreased area fraction of staining, power coherence is applicable when examining fibers that are disrupted due to residual effects of axon injury. Coherence shows evidence of chronic white matter injury, which has been found as late as 60 days following repetitive traumatic brain injury in a mouse model (Donovan et al., 2014). Furthermore, coherence is advantageous because of its ability to differentiate between complex fibers and injured fibers, a well-known dilemma encountered in the single tensor model of diffusion imaging (Arfanakis et al., 2002; Behrens et al., 2014; Pierpaoli et al., 1996). The single tensor model used in DTI results in complex fibers and injured fibers being indistinguishable by metrics such as fractional anisotropy (Arfanakis et al., 2002; Behrens et al., 2014; Yeh et al., 2010) but readily addressed with GQI and other

more advanced diffusion imaging methods (Yeh et al., 2010). Application of power coherence to histological measures may be able help to resolve the interpretation of diffusion imaging signals in otherwise ambiguous situations, particularly in regions where injury occurs in white matter regions that have crossing fibers.

A second major advantage of this study is the high quality of the diffusion MRI data, notably the high spatial resolution (250 μm × 250 μm in plane) and high angular resolution of the GQI data (202 directions). The optimized spatial and angular resolutions were key during the validation by comparing fiber orientation on a voxel-wise basis. Our method of calculating fiber orientation using the two dimensional Fourier transform was successful because of its ability to discern between crossing and simple fiber populations at these high spatial resolutions. Implementation of a two dimensional Fourier transformation, which does not take into account the fiber orientation of the surrounding voxels was also complementary to the GQI reconstruction method, where fiber orientations within a single MRI voxel are based solely on the diffusion of water within that single voxel. At lower spatial resolutions, such as those approaching clinically feasible levels, application of the Fourier transformation to validate tractography would be challenging in complex white matter regions (Budde and Frank, 2012; Budde et al., 2011). Furthermore, the measure of power coherence used here to distinguish between disrupted and crossing fibers would no longer be applicable due to signal averaging within a larger voxel volume. We have shown that the true heterogeneity of cortical white matter is lost at lower resolutions, a factor which must be considered if performing radiological pathological correlations in a disease where the primary pathology is located in such complex white matter regions. While this finding is not surprising, it does make explicit the need for either alternative imaging modalities that can provide clinically achievable high spatial resolutions, or the development of an injury specific imaging marker which would allow for more sensitive diagnostic imaging at current spatial resolutions.

We must also consider the limitations of our registration method. First, manual landmark placement is an inherent source of variability in registration, and would be increasingly difficult at low resolutions where the gray/white matter boundary and anatomical features become less visually salient (Choe et al., 2011). An additional confound of our landmark based registration method is that registration is most accurate in a region with a high density of landmarks, and may be more prone to errors in regions with sparse landmark placement, or in regions far away from the landmarks. Therefore, further validation steps should be considered, such as evaluating the accuracy of registration as a function of distance from landmarks placed along the gray/white matter boundary and tissue boundary. Second, because the workflow is a two dimensional registration, any correlation analysis that uses our technique is limited to in plane histological features. When considering three dimensional histology to MRI registration, parameters such as inter-slice sampling interval and tissue sectioning thickness would need to be optimized (Absinta et al., 2014; Breen et al., 2005b; Goubran et al., 2013; Zarow et al., 2004) because of rapid changes in tissue architecture between slices. At high spatial resolutions and small slice thicknesses, validation of three dimensional histological registration could then be performed using three dimensional structure tensor analysis (Schilling et al., 2016). Despite this possibility, the z-axis changes between MRI slices may not be able to be sufficiently accounted for using current imaging resolutions, particularly in human cortical tissue where sulci change or even

disappear within our current 500 μm slice thickness. These rapid z-axis changes would create challenges when attempting to register and match histological sections with the associated MRI slices. Our current validation method of determining the correlation of fiber direction is therefore only valid when considering features that are in the histological plane. While there may be agreement between in plane fiber orientations, the strongest evidence of robust 3D coregistration would be correlation of fibers that have a primary directional component along the z-axis. Aligned to the issue of three dimensional coregistration and validation is the application power coherence to distinguish between disrupted white matter and fibers that are perpendicular to the plane of histology. In this study, we limited our analyses to voxels with in plane major fiber components, using GQI data to identify voxels with primary or secondary fiber components perpendicular to the plane of histology. Without this exclusionary criteria, using power coherence is not sufficient to distinguish between disrupted and intact white matter which is out of plane. Using a technique such as serial two photon microscopy, where the tissue section is imaged below the block surface before sectioning would prevent the issues of z-axis warping that commonly occurs in the serial sectioning method that we have used here (Amato et al., 2016). Alternatively, an approach such as CLARITY (Chung and Deisseroth, 2013) combined with a stain for myelinated fibers would be able to distinguish between out of plane, intact and disrupted white matter. Third, while we have been able to show that complex fiber orientations can be discerned using quantitative histology methods, there may be a dependency, yet to be characterized, on the quality of the *ex vivo* tissue, fixation methods, and post-mortem interval. Finally, while our coregistration has been extensively validated in white matter, this approach has not been fully validated for complex gray matter.

The most immediate applications of our registration method are in the field of radiological-pathological correlations in CTE (Holleran et al., 2015), exploring the relationship between multiple immunohistochemistry stained markers and associated advanced diffusion MRI metrics. The workflow is also applicable to analysis *in vivo* using animal models of concussive injury, by scanning living animals and performing registration and subsequent correlation after sacrificing the animals. Because we have shown that histology-MRI registration is highly robust in human tissue, *ex vivo* correlation studies may potentially be conducted in cases of acute traumatic brain injury, where pathology is drastically different compared to chronic cases. Further applications of this method could be extended to *ex vivo* correlations in Alzheimer's Disease, frontotemporal dementia, or Parkinson's disease (Suri et al., 2014), where the neuropathology is distinct but the effect on traditional and advanced diffusion MRI metrics needs to be further elucidated.

Supplementary Material

Refer to Web version on PubMed Central for supplementary material.

Acknowledgments

References

Absinta M, Nair G, Filippi M, Ray-Chaudhury A, Reyes-Mantilla MI, Pardo CA, Reich DS. Postmortem magnetic resonance imaging to guide the pathologic cut: individualized, 3-dimensionally printed cutting boxes for fixed brains. J Neuropathol Exp Neurol. 2014; 73:780–788. [PubMed: 25007244]

Amato SP, Pan F, Schwartz J, Ragan TM. Whole Brain Imaging with Serial Two-Photon Tomography. Front Neuroanat. 2016; 10:31. [PubMed: 27047350]

Arfanakis K, Haughton VM, Carew JD, Rogers BP, Dempsey RJ, Meyerand ME. Diffusion tensor MR imaging in diffuse axonal injury. AJNR Am J Neuroradiol. 2002; 23:794–802. [PubMed: 12006280]

Barrio JR, Small GW, Wong KP, Huang SC, Liu J, Merrill DA, Giza CC, Fitzsimmons RP, Omalu B, Bailes J, Kepe V. In vivo characterization of chronic traumatic encephalopathy using [F-18]FDDNP PET brain imaging. Proc Natl Acad Sci U S A. 2015; 112:E2039–2047. [PubMed: 25848027]

Behrens, TEJ., Sotiropoulos, SN., Jbabdi, S. Diffusion MRI. 2. Academic Press; San Diego: 2014. Chapter 19 - MR Diffusion Tractography; p. 429-451.

Bennett RE, Mac Donald CL, Brody DL. Diffusion tensor imaging detects axonal injury in a mouse model of repetitive closed-skull traumatic brain injury. Neuroscience letters. 2012; 513:160–165. [PubMed: 22343314]

Blumbergs PC, Jones NR, North JB. Diffuse axonal injury in head trauma. J Neurol Neurosurg Psychiatry. 1989; 52:838–841. [PubMed: 2769276]

Blumbergs PC, Scott G, Manavis J, Wainwright H, Simpson DA, McLean AJ. Staining of amyloid precursor protein to study axonal damage in mild head injury. Lancet. 1994; 344:1055–1056. [PubMed: 7523810]

Bogoslovsky T, Wilson D, Chen Y, Hanlon D, Gill J, Jeromin A, Song L, Moore C, Gong Y, Kenney K, Diaz-Arrastia R. Increases of Plasma Levels of Glial Fibrillary Acidic Protein, Tau, and Amyloid beta up to 90 Days after Traumatic Brain Injury. Journal of Neurotrauma. 2016

Breen MS, Lancaster TL, Wilson DL. Correcting spatial distortion in histological images. Comput Med Imaging Graph. 2005a; 29:405–417. [PubMed: 16006097]

Breen MS, Lazebnik RS, Wilson DL. Three-dimensional registration of magnetic resonance image data to histological sections with model-based evaluation. Ann Biomed Eng. 2005b; 33:1100–1112. [PubMed: 16133918]

Brody DL, Mac Donald C, Kessens CC, Yuede C, Parsadanian M, Spinner M, Kim E, Schwetye KE, Holtzman DM, Bayly PV. Electromagnetic controlled cortical impact device for precise, graded experimental traumatic brain injury. Journal of Neurotrauma. 2007; 24:657–673. [PubMed: 17439349]

Budde MD, Annese J. Quantification of anisotropy and fiber orientation in human brain histological sections. Front Integr Neurosci. 2013; 7:3. [PubMed: 23378830]

Budde MD, Frank JA. Examining brain microstructure using structure tensor analysis of histological sections. Neuroimage. 2012; 63:1–10. [PubMed: 22759994]

Budde MD, Janes L, Gold E, Turtzo LC, Frank JA. The contribution of gliosis to diffusion tensor anisotropy and tractography following traumatic brain injury: validation in the rat using Fourier analysis of stained tissue sections. Brain. 2011; 134:2248–2260. [PubMed: 21764818]

Choe AS, Gao Y, Li X, Compton KB, Stepniewska I, Anderson AW. Accuracy of image registration between MRI and light microscopy in the ex vivo brain. Magn Reson Imaging. 2011; 29:683–692. [PubMed: 21546191]

Chung K, Deisseroth K. CLARITY for mapping the nervous system. Nature methods. 2013; 10:508–513. [PubMed: 23722210]

D'Arceuil HE, Westmoreland S, de Crespigny AJ. An approach to high resolution diffusion tensor imaging in fixed primate brain. Neuroimage. 2007; 35:553–565. [PubMed: 17292630]

Dauguet J, Delzescaux T, Conde F, Mangin JF, Ayache N, Hantraye P, Frouin V. Three-dimensional reconstruction of stained histological slices and 3D non-linear registration with in-vivo MRI for whole baboon brain. J Neurosci Methods. 2007; 164:191–204. [PubMed: 17560659]

Deroulers C, Ameisen D, Badoual M, Gerin C, Granier A, Lartaud M. Analyzing huge pathology images with open source software. Diagnostic pathology. 2013; 8:92. [PubMed: 23829479]

Donahue CJ, Sotiropoulos SN, Jbabdi S, Hernandez-Fernandez M, Behrens TE, Dyrby TB, Coalson T, Kennedy H, Knoblauch K, Van Essen DC, Glasser MF. Using Diffusion Tractography to Predict Cortical Connection Strength and Distance: A Quantitative Comparison with Tracers in the Monkey. The Journal of neuroscience: the official journal of the Society for Neuroscience. 2016; 36:6758–6770. [PubMed: 27335406]

Donovan V, Kim C, Anugerah AK, Coats JS, Oyoyo U, Pardo AC, Obenaus A. Repeated mild traumatic brain injury results in long-term white-matter disruption. Journal of cerebral blood flow and metabolism: official journal of the International Society of Cerebral Blood Flow and Metabolism. 2014; 34:715–723.

Edgar, JM., Griffiths, IR. Diffusion MRI. 2. Academic Press; San Diego: 2014. Chapter 7 - White Matter Structure: A Microscopist's View; p. 127-153.

Gangolli, M., Kim, J., Holleran, L., Stein, T., Alvarez, V., McKee, A., Brody, D. Advanced Diffusion MRI Methods to Quantitatively Distinguish Between Complex White Matter and Traumatic Axonal Injury; National Neurotrauma Symposium; Santa Fe, NM: Mary Ann Liebert; 2015. p. A54

Gonzalez, RC., Woods, RE., Eddins, SL. Digital Image processing using MATLAB. 2. Gatesmark Pub; S.I: 2009.

Goshtasby A. Image Registration by Local Approximation Methods. Image and Vision Computing. 1988; 6:255–261.

Goubran M, Crukley C, de Ribaupierre S, Peters TM, Khan AR. Image registration of ex-vivo MRI to sparsely sectioned histology of hippocampal and neocortical temporal lobe specimens. Neuroimage. 2013; 83:770–781. [PubMed: 23891884]

Goubran M, de Ribaupierre S, Hammond RR, Currie C, Burneo JG, Parrent AG, Peters TM, Khan AR. Registration of in-vivo to ex-vivo MRI of surgically resected specimens: a pipeline for histology to in-vivo registration. J Neurosci Methods. 2015; 241:53–65. [PubMed: 25514760]

Hagmann P, Jonasson L, Deffieux T, Meuli R, Thiran JP, Wedeen VJ. Fibertract segmentation in position orientation space from high angular resolution diffusion MRI. Neuroimage. 2006; 32:665–675. [PubMed: 16815713]

Herrera JJ, Bockhorst K, Kondraganti S, Stertz L, Quevedo J, Narayana PA. Acute White Matter Tract Damage after Frontal Mild Traumatic Brain Injury. J Neurotrauma. 2016

Holleran, L., Kim, J., Gangolli, M., Stein, T., Alvarez, V., McKee, A., Brody, D. Advanced Diffusion MRI-Based Radiological Pathological Correlations in Chronic Traumatic Encephalopathy. National Neurotrauma Symposium; Santa Fe, NM: Mary Ann Liebert; 2015. p. A9

Hubbard, PL., Parker, GJM. Diffusion MRI. 2. Academic Press; San Diego: 2014. Chapter 20 - Validation of Tractography; p. 453-480.

Jeurissen B, Leemans A, Tournier JD, Jones DK, Sijbers J. Investigating the prevalence of complex fiber configurations in white matter tissue with diffusion magnetic resonance imaging. Human brain mapping. 2013; 34:2747–2766. [PubMed: 22611035]

Johnson VE, Stewart JE, Begbie FD, Trojanowski JQ, Smith DH, Stewart W. Inflammation and white matter degeneration persist for years after a single traumatic brain injury. Brain. 2013; 136:28–42. [PubMed: 23365092]

Jones DK, Cercignani M. Twenty-five pitfalls in the analysis of diffusion MRI data. NMR in biomedicine. 2010; 23:803–820. [PubMed: 20886566]

Jones DK, Horsfield MA, Simmons A. Optimal strategies for measuring diffusion in anisotropic systems by magnetic resonance imaging. Magnetic resonance in medicine. 1999; 42:515–525. [PubMed: 10467296]

Kier EL, Staib LH, Davis LM, Bronen RA. Anatomic dissection tractography: a new method for precise MR localization of white matter tracts. AJNR Am J Neuroradiol. 2004; 25:670–676. [PubMed: 15140704]

Kim JH, Trinkaus K, Ozcan A, Budde MD, Song SK. Postmortem delay does not change regional diffusion anisotropy characteristics in mouse spinal cord white matter. NMR in biomedicine. 2007; 20:352–359. [PubMed: 17451177]

Lazebnik RS, Lancaster TL, Breen MS, Lewin JS, Wilson DL. Volume registration using needle paths and point landmarks for evaluation of interventional MRI treatments. IEEE Trans Med Imaging. 2003; 22:653–660. [PubMed: 12846434]

Le Bihan D. Molecular diffusion, tissue microdynamics and microstructure. NMR Biomed. 1995; 8:375–386. [PubMed: 8739274]

Mac Donald CL, Dikranian K, Song SK, Bayly PV, Holtzman DM, Brody DL. Detection of traumatic axonal injury with diffusion tensor imaging in a mouse model of traumatic brain injury. Exp Neurol. 2007; 205:116–131. [PubMed: 17368446]

McKee AC, Cairns NJ, Dickson DW, Folkerth RD, Keene CD, Litvan I, Perl DP, Stein TD, Vonsattel JP, Stewart W, Tripodis Y, Crary JF, Bieniek KF, Dams-O'Connor K, Alvarez VE, Gordon WA. The first NINDS/NIBIB consensus meeting to define neuropathological criteria for the diagnosis of chronic traumatic encephalopathy. Acta neuropathologica. 2016; 131:75–86. [PubMed: 26667418]

McKee AC, Cantu RC, Nowinski CJ, Hedley-Whyte ET, Gavett BE, Budson AE, Santini VE, Lee HS, Kubilus CA, Stern RA. Chronic traumatic encephalopathy in athletes: progressive tauopathy after repetitive head injury. J Neuropathol Exp Neurol. 2009; 68:709–735. [PubMed: 19535999]

McKee AC, Stein TD, Kiernan PT, Alvarez VE. The neuropathology of chronic traumatic encephalopathy. Brain Pathol. 2015; 25:350–364. [PubMed: 25904048]

McKee AC, Stern RA, Nowinski CJ, Stein TD, Alvarez VE, Daneshvar DH, Lee HS, Wojtowicz SM, Hall G, Baugh CM, Riley DO, Kubilus CA, Cormier KA, Jacobs MA, Martin BR, Abraham CR, Ikezu T, Reichard RR, Wolozin BL, Budson AE, Goldstein LE, Kowall NW, Cantu RC. The spectrum of disease in chronic traumatic encephalopathy. Brain: a journal of neurology. 2013; 136:43–64. [PubMed: 23208308]

Miller KL, Stagg CJ, Douaud G, Jbabdi S, Smith SM, Behrens TE, Jenkinson M, Chance SA, Esiri MM, Voets NL, Jenkinson N, Aziz TZ, Turner MR, Johansen-Berg H, McNab JA. Diffusion imaging of whole, postmortem human brains on a clinical MRI scanner. Neuroimage. 2011; 57:167–181. [PubMed: 21473920]

Mitsis EM, Riggio S, Kostakoglu L, Dickstein DL, Machac J, Delman B, Goldstein M, Jennings D, D'Antonio E, Martin J, Naidich TP, Aloysi A, Fernandez C, Seibyl J, DeKosky ST, Elder GA, Marek K, Gordon W, Hof PR, Sano M, Gandy S. Tauopathy PET and amyloid PET in the diagnosis of chronic traumatic encephalopathies: studies of a retired NFL player and of a man with FTD and a severe head injury. Translational psychiatry. 2014; 4:e441. [PubMed: 25226550]

Nazaran A, Wisco JJ, Hageman N, Schettler SP, Wong A, Vinters HV, Teng CC, Bangerter NK. Methodology for computing white matter nerve fiber orientation in human histological slices. Journal of neuroscience methods. 2016; 261:75–84. [PubMed: 26709015]

Niogi SN, Mukherjee P, Ghajar J, Johnson C, Kolster RA, Sarkar R, Lee H, Meeker M, Zimmerman RD, Manley GT, McCandliss BD. Extent of microstructural white matter injury in postconcussive syndrome correlates with impaired cognitive reaction time: a 3T diffusion tensor imaging study of mild traumatic brain injury. AJNR Am J Neuroradiol. 2008; 29:967–973. [PubMed: 18272556]

Pierpaoli C, Barnett A, Pajevic S, Chen R, Penix LR, Virta A, Basser P. Water diffusion changes in Wallerian degeneration and their dependence on white matter architecture. Neuroimage. 2001; 13:1174–1185. [PubMed: 11352623]

Pierpaoli C, Jezzard P, Basser PJ, Barnett A, Di Chiro G. Diffusion tensor MR imaging of the human brain. Radiology. 1996; 201:637–648. [PubMed: 8939209]

Prins N, Kingdom FA. Detection and discrimination of texture modulations defined by orientation, spatial frequency, and contrast. J Opt Soc Am A Opt Image Sci Vis. 2003; 20:401–410. [PubMed: 12630826]

Reveley C, Seth AK, Pierpaoli C, Silva AC, Yu D, Saunders RC, Leopold DA, Ye FQ. Superficial white matter fiber systems impede detection of long-range cortical connections in diffusion MR tractography. Proceedings of the National Academy of Sciences of the United States of America. 2015; 112:E2820–2828. [PubMed: 25964365]

Rutgers DR, Toulgoat F, Cazejust J, Fillard P, Lasjaunias P, Ducreux D. White matter abnormalities in mild traumatic brain injury: a diffusion tensor imaging study. AJNR Am J Neuroradiol. 2008; 29:514–519. [PubMed: 18039754]

Ryu J, Horkayne-Szakaly I, Xu L, Pletnikova O, Leri F, Eberhart C, Troncoso JC, Koliatsos VE. The problem of axonal injury in the brains of veterans with histories of blast exposure. Acta Neuropathol Commun. 2014; 2:153. [PubMed: 25422066]

Savaskan NE, Weinmann O, Heimrich B, Eyupoglu IY. High resolution neurochemical gold staining method for myelin in peripheral and central nervous system at the light- and electron-microscopic level. Cell Tissue Res. 2009; 337:213–221. [PubMed: 19513756]

Schilling K, Janve V, Gao Y, Stepniewska I, Landman BA, Anderson AW. Comparison of 3D orientation distribution functions measured with confocal microscopy and diffusion MRI. Neuroimage. 2016; 129:185–197. [PubMed: 26804781]

Shattuck DW, Leahy RM. BrainSuite: an automated cortical surface identification tool. Medical image analysis. 2002; 6:129–142. [PubMed: 12045000]

Stern RA, Daneshvar DH, Baugh CM, Seichepine DR, Montenigro PH, Riley DO, Fritts NG, Stamm JM, Robbins CA, McHale L, Simkin I, Stein TD, Alvarez VE, Goldstein LE, Budson AE, Kowall NW, Nowinski CJ, Cantu RC, McKee AC. Clinical presentation of chronic traumatic encephalopathy. Neurology. 2013; 81:1122–1129. [PubMed: 23966253]

Strich SJ. Diffuse degeneration of the cerebral white matter in severe dementia following head injury. J Neurol Neurosurg Psychiatry. 1956; 19:163–185. [PubMed: 13357957]

Suri S, Topiwala A, Mackay CE, Ebmeier KP, Filippini N. Using structural and diffusion magnetic resonance imaging to differentiate the dementias. Current neurology and neuroscience reports. 2014; 14:475. [PubMed: 25030502]

Thelwall PE, Shepherd TM, Stanisz GJ, Blackband SJ. Effects of temperature and aldehyde fixation on tissue water diffusion properties, studied in an erythrocyte ghost tissue model. Magnetic resonance in medicine. 2006; 56:282–289. [PubMed: 16841346]

Wang Y, Sun P, Wang Q, Trinkaus K, Schmidt RE, Naismith RT, Cross AH, Song SK. Differentiation and quantification of inflammation, demyelination and axon injury or loss in multiple sclerosis. Brain: a journal of neurology. 2015; 138:1223–1238. [PubMed: 25724201]

Weiss M, Alkemade A, Keuken MC, Muller-Axt C, Geyer S, Turner R, Forstmann BU. Spatial normalization of ultrahigh resolution 7 T magnetic resonance imaging data of the postmortem human subthalamic nucleus: a multistage approach. Brain Struct Funct. 2015; 220:1695–1703. [PubMed: 24663802]

White E, Woolley M, Bienemann A, Johnson DE, Wyatt M, Murray G, Taylor H, Gill SS. A robust MRI-compatible system to facilitate highly accurate stereotactic administration of therapeutic agents to targets within the brain of a large animal model. Journal of neuroscience methods. 2011; 195:78–87. [PubMed: 21074564]

Wiegell MR, Larsson HB, Wedeen VJ. Fiber crossing in human brain depicted with diffusion tensor MR imaging. Radiology. 2000; 217:897–903. [PubMed: 11110960]

Yeh FC, Wedeen VJ, Tseng WY. Generalized q-sampling imaging. IEEE Trans Med Imaging. 2010; 29:1626–1635. [PubMed: 20304721]

Zagorchev L, Goshtasby A. A comparative study of transformation functions for nonrigid image registration. IEEE transactions on image processing: a publication of the IEEE Signal Processing Society. 2006; 15:529–538. [PubMed: 16519341]

Zarow C, Kim TS, Singh M, Chui HC. A standardized method for brain-cutting suitable for both stereology and MRI-brain co-registration. J Neurosci Methods. 2004; 139:209–215. [PubMed: 15488234]

Zemmoura I, Serres B, Andersson F, Barantin L, Tauber C, Filipiak I, Cottier JP, Venturini G, Destrieux C. FIBRASCAN: a novel method for 3D white matter tract reconstruction in MR space from cadaveric dissection. Neuroimage. 2014; 103:106–118. [PubMed: 25234114]

Appendix I: Calculation of fiber orientation and coherence

Orientation and coherence were calculated as previously described (Budde et al., 2011; Gonzalez et al., 2009; Prins and Kingdom, 2003) using a two dimensional discrete Fourier transformation. Each grayscale region of interest of size M × N pixels can be described in terms of spatial frequencies using the formula

$$F(u,v) = \sum_{x=0}^{M-1} \sum_{y=0}^{N-1} f(x,y) e^{-i2\pi(ux/M + vy/N)}$$
(Eq. 5)

Where x and y are the pixel coordinates in the spatial domain, u and v are the corresponding frequency components and $i = \sqrt{-1}$ Because we are not sampling infinitely and there is a baseline level of background intensity, there will be false peaks due to edge effects and mean pixel intensity in the Fourier domain. Consequently, each region of interest in the spatial domain must be zero mean normalized and windowed by multiplying the region with a Tukey window described as

$$\omega_0 = \left\{ \begin{array}{cc} 1 & r < \frac{(1-\alpha)N+1}{2} \\ \frac{1}{2}[1 + \cos(\frac{2r-1}{\alpha N} - \frac{1}{\alpha} + 1)] & \frac{(1-\alpha)N+1}{2} \leq r < \frac{N+1}{2} \\ 0 & \frac{N+1}{2} \leq r \end{array} \right\}$$
(Eq. 6)

where α represents the tapering of the window between 0 and 1, selected to maximize the sharpness of power spectra peaks for most efficient extraction of orientations, and r is defined by

$$r = \sqrt{\left(x - \frac{M-1}{2}\right)^2 + \left(y - \frac{N-1}{2}\right)^2}$$
(Eq. 7)

The power spectrum can then be calculated using

$$P(u,v) = \left| F(u,v)^2 \right| = R^2(u,v) + I^2(u,v)$$
(Eq. 8)

where R(u, v) and I(u, v) are the real and imaginary components of the spatial frequencies.

After fitting the resulting power spectrum with two ellipses in ImageJ and measuring preferential and radial axes of both ellipses, the power coherence of each ROI was calculated as

$$1 - \frac{\lambda_2 + \lambda_4}{\lambda_1 + \lambda_3} \quad \text{(Eq. 9)}$$

Where λ_1, λ_3 are the preferential axes of the ellipses and λ_2, λ_4 are the radial axes of the ellipses. Power coherence was calculated to be a metric between 0 and 1, where reduced power coherence reflects reduced fiber integrity. Fiber orientation was measured as the angle between the preferential axes of the ellipses and the horizontal, adding 90° to account for the power spectrum rotation in the frequency domain and rotation of each voxel to the orientation measured from the elliptical fit.

Highlights

- A nonlinear histology-MRI coregistration method is proposed

- Quantitative correlations of fiber orientation validate registration accuracy

- Disrupted white matter is quantitatively distinct from complex white matter
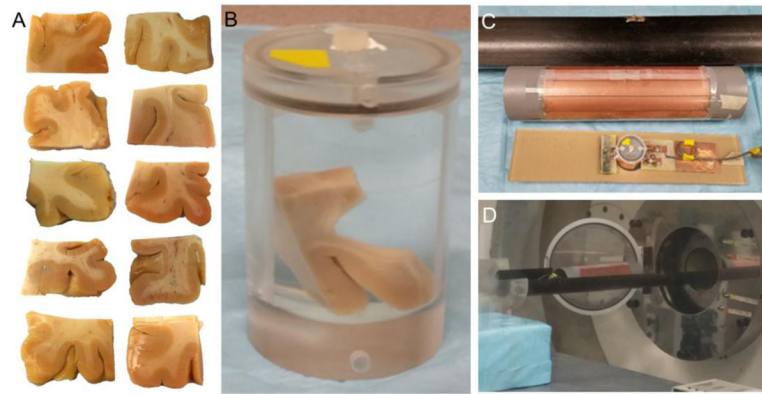
Fig. 1. MRI data acquisition
A. Ten human *ex vivo* tissue samples from the superior frontal cortex (BA 8/9) were requilibrated at 4°Celsius in 1xPBS with 0.01% NaN_3 for two weeks after being received from Boston University. Prior to MRI data acquisition, tissue was stored overnight at room temperature in Fluorinert. **B.** Tissue was placed in a container which optimized filling factor thereby maximizing the tissue signal. **C.** An inductive coupling coil was used to in order to better tune the coil and tissue contained contents to the resonant frequency of the MRI scanner. **D.** GQI data were acquired in an 11.74 T Agilent MRI scanner, requiring a total scan time of 11 hours per tissue sample.
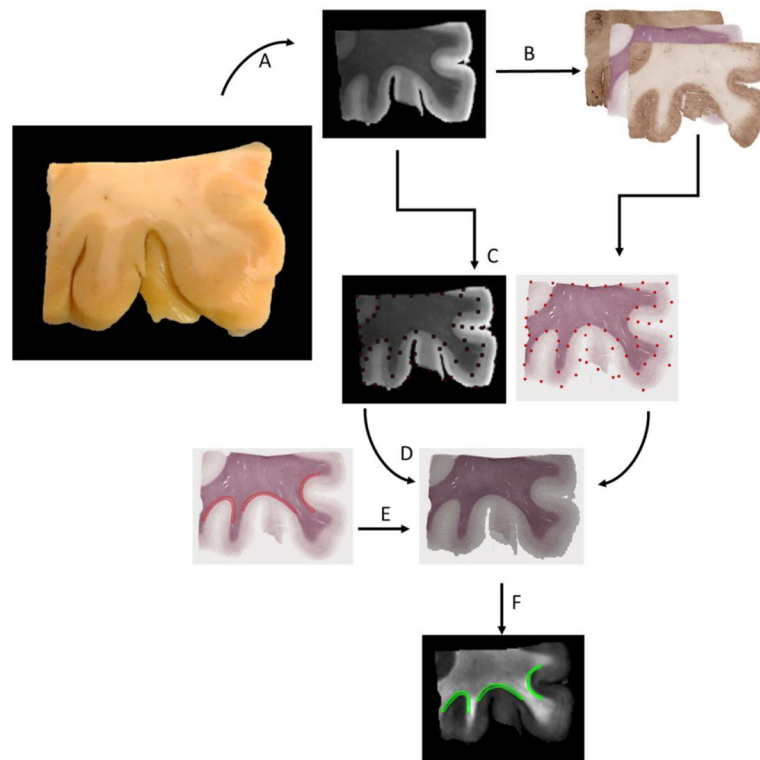
**Fig. 2. Workflow of histology to MRI registration**

A. Fixed blocks of human cortical tissue were scanned using a spin echo sequence to collect GQI data. **B.** Tissue was sectioned into serial 50 μm thick sections and stained for neuropathological markers. Every sixth section (250 μm spacing) was stained for myelin using Black Gold II, and digital images of histology were acquired for quantification. **C.** Landmarks were manually placed on the digital image (downsampled to x5 magnification) of the Black Gold II image and associated slice on the unweighted diffusion (b = 0 s/mm^2) data in corresponding locations. **C.** A nonlinear least squares registration was applied to warp the histological image to the same orientation and dimensions as MRI space. **D.** To preserve high resolution needed for further quantitative histology, an inverse transformation was applied to each warped histological voxel to generate a grid of ROIs where each region of interest represents a voxel of the diffusion data. **E.** ROIs were then able to be drawn on the high resolution (x5 magnification) histology. **F.** Using the voxel based grid as a reference, the corresponding ROIs were automatically selected on the MRI data for other investigations of radiological-pathological correlations in specific zones such as sub-sulcal white matter (Holleran et al., 2015).
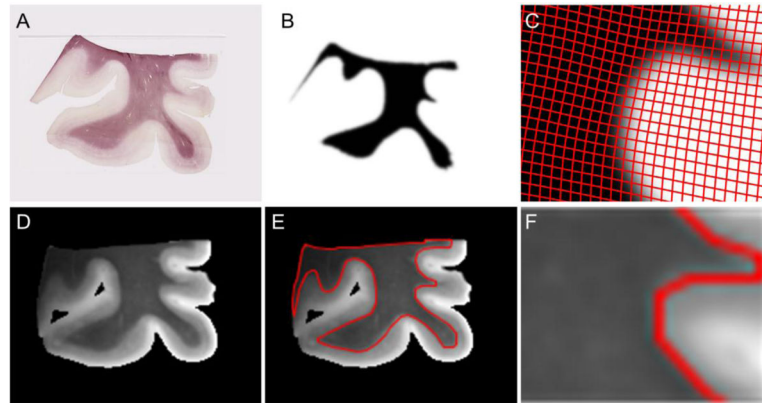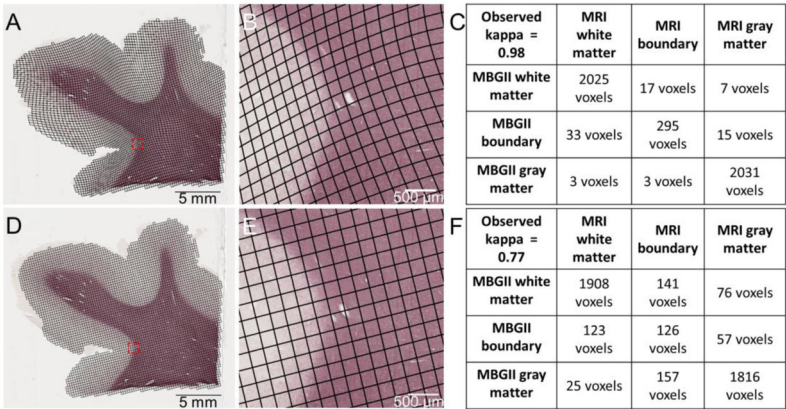
Fig. 3. Automated generation of white matter masks
A. Histologically derived white matter masks were automatically generated using the high gray white matter contrast of the Black Gold II stain. **B.** Sections were thresholded and blurred using a Gaussian filter with a radius matching the MRI in plane resolution (250 μm). **C.** The corresponding voxel-based grid was then overlaid onto the blurred mask. Voxel equivalent ROIs with a mean value of 1 (darkest intensity) were classified as white matter, while voxels with a mean value of 0 (lightest intensity) were classified as gray matter. Voxels with a mean intensity between 0 and 1 were classified as gray/white matter boundary. **D.** MRI voxel classification was based on the unweighted diffusion image ($b = 0$ s/mm^2). **E.** The boundary between gray and white matter was selected using the edge detection feature available in ImageJ. **F.** Voxels within this boundary were classified as white matter, voxels outside of this boundary were classified as gray matter, and voxels selected during edge detection were classified as boundary voxels.
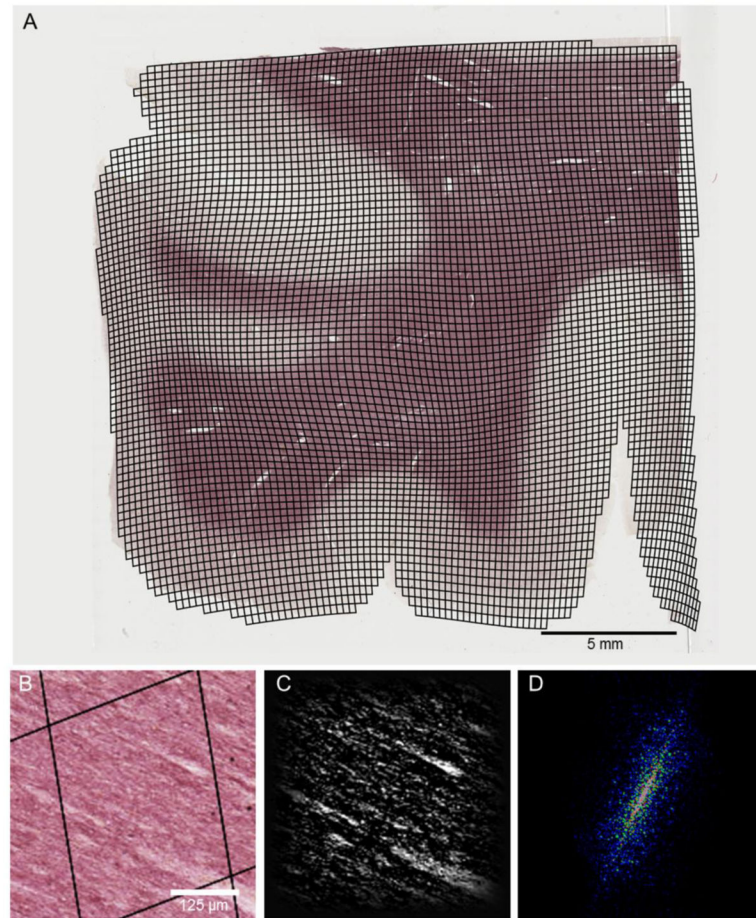
Fig. 4. Derivation of fiber orientation from histology
A. Voxel-based grids derived from nonlinear least squares registration were overlaid onto the corresponding Black Gold II stained tissue sections in ImageJ. **B.** Each white matter voxel was used as a region of interest. **C.** The ROI equivalent to each voxel was converted to grayscale, zero mean normalized and windowed to remove edge and center spike artifacts. **D.** The power spectrum resulting from a two dimensional discrete Fourier transformation shows high amplitude peaks perpendicular to fiber orientation stained by Black Gold II. Intensity of the power spectrum corresponds to the amplitude in dB at each spatial frequency. In this example, the power spectrum has greatest amplitude at approximately 60 degrees from the horizontal, perpendicular to the fibers in the spatial domain which are oriented at approximately −30 degrees; the direction of maximum change in signal amplitude is perpendicular to the fiber orientation.

A. A nonlinear moving last squares transformation was used to generate voxel-based grids corresponding to Black Gold II sections.

B. Variation in tissue warping is apparent by the non-uniform shape of the grid in gray and matter regions.

Observed kappa = 0.98	MRI white matter	MRI boundary	MRI gray matter
MBGII white matter	2025 voxels	17 voxels	7 voxels
MBGII boundary	33 voxels	295 voxels	15 voxels
MBGII gray matter	3 voxels	3 voxels	2031 voxels

| Observed kappa = 0.77	MRI white matter	MRI boundary	MRI gray matter
MBGII white matter	1908 voxels	141 voxels	76 voxels
MBGII boundary	123 voxels	126 voxels	57 voxels
MBGII gray matter	25 voxels	157 voxels	1816 voxels

Fig. 5. Comparison of nonlinear vs linear transformation methods

A. A nonlinear moving last squares transformation was used to generate voxel-based grids corresponding to Black Gold II sections. **B.** Variation in tissue warping is apparent by the non-uniform shape of the grid in gray and matter regions. **C.** An unweighted Cohen's kappa coefficient was used to evaluate the agreement of voxels classified as white matter, gray matter, or boundary voxels using histology and MRI, resulting in very strong agreement (kappa = 0.98). **D.** An affine transformation was used to generate voxel-based grids using the same manually placed landmarks as the nonlinear transformations. **E.** Uniform warping across gray and white matter is apparent, particularly at the gray/white matter boundary. **F.** The unweighted kappa coefficient was calculated, resulting in good agreement (kappa = 0.77), but there is a large discrepancy in the agreement between boundary voxels, indicating that a linear transformation may not be able to account for sudden variations in tissue.
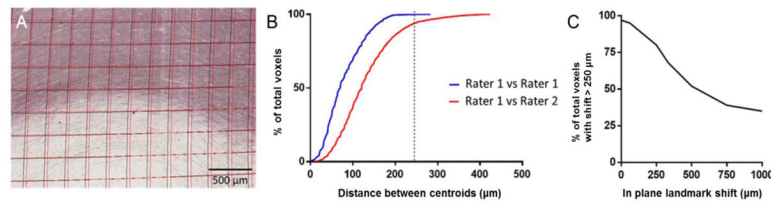
Fig. 6. Reliability testing

A. Two grids were generated and overlaid onto the corresponding histological images based on two sets of landmarks placed by either the same or two different users. **B.** The cumulative histogram of the distance the centroid of each voxel has shifted shows that even when two different users have placed separate sets of fiducials based on anatomical landmarks, less than 25% of voxels have shifted more than 250 μm, a threshold determined using the MRI in plane resolution. **C.** A simulation was carried out to test the robustness of nonlinear registration to variations in landmark placement. The percentage of voxels that had shifted less than the MRI in plane resolution (250 μm) was then plotted as a function of the maximum distance the landmarks had been shifted. Registration is less prone to variability when landmarks have been shifted less than 350 μm, with 80% of voxels having shifted less than 250 μm.
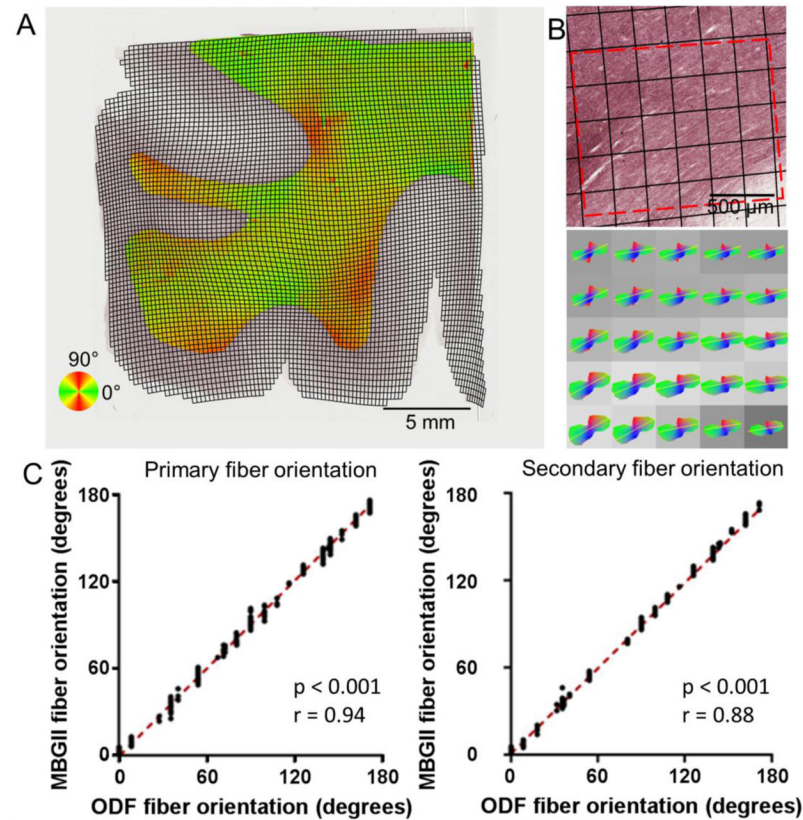
Fig. 7. Correlation of diffusion based and histologically based fiber orientation
A. Fitting two tensors to the power spectrum of each white matter voxel-registered ROI
resulted in a directionality map, where the color of each registered region of interest
represents the orientation of the primary fiber population. **B.** Directionality comparisons
could then be directly made by comparing the histologically derived fiber orientation from
the Myelin Black Gold II with the GQI derived orientation. **C.** There was a strong nearly
one-to-one linear relationship between the quantitative histological metric and the GQI data
(red line indicates line of identity). Orientations calculated from the ODFs resulted in
discrete bins due to the finite angular resolution of the GQI data (202 directions) on the x-
axis, while the Black Gold II based fiber orientations were a continuous measure. Therefore,
a one-tailed Spearman's correlation was used, resulting in p values < 0.001 for both primary
and secondary major fiber components.
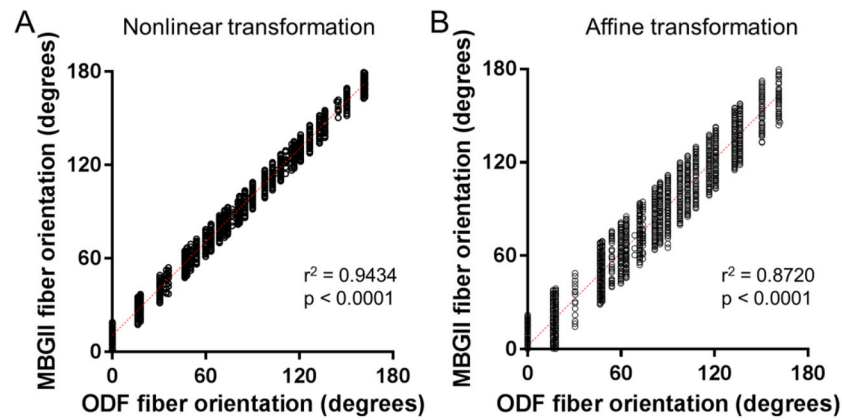
Fig. 8. Performance of nonlinear vs affine transformations when correlating fiber orientation
A. Nonlinear transformation results in a linear relationship, determined using a linear regression analysis (p < 0.0001, $r^2 = 0.94$) of ODF derived vs Black Gold II derived primary fiber orientations. Red line indicates the fitted line. **B.** Affine transformation of the same data also results in a strong linear relationship, based on linear regression analysis (p < 0.0001, $r^2 = 0.87$), but the distribution of Black Gold II fiber orientation in each ODF bin is wider compared to the results of the nonlinear transformation. A difference test shows that the correlation of the primary fiber orientations resulting from a nonlinear transformation is superior to the correlation resulting from an affine transformation. The maximum difference between the primary in plane peak of the ODF and the secondary in plane peak of the ODF was 153.73°.
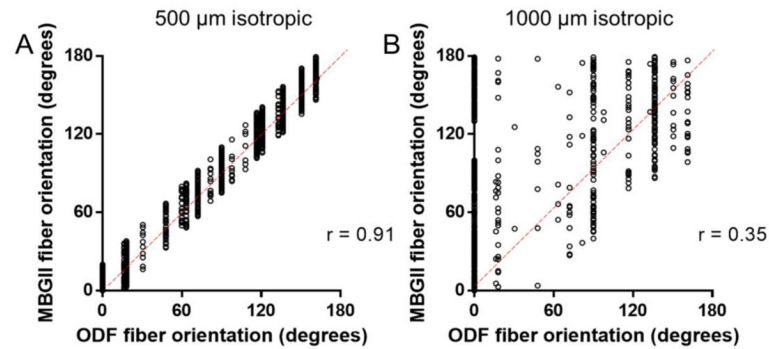
**Fig. 9. Relationship between spatial resolution and fiber direction correlations**
A. Comparison of ODF derived and Black Gold II derived fiber orientations at 500 μm isotropic resolution in complex cortical white matter continues to show a strong correlation (r = 0.91) but the distribution of histologically based fiber orientations is broader for each bin, indicating that a two tensor fit may not be able to account for the increased voxel wise white matter heterogeneity. Red line indicates line of identity. **B.** Comparison of ODF derived and Black Gold II derived fiber orientations at 1000 μm isotropic resolution shows a low correlation (r = 0.35), where the ability to implement the 2D FFT to discern between simple, crossing, and disrupted white matter is lost, showing the limitations of a two tensor model. Red line indicates line of identity.
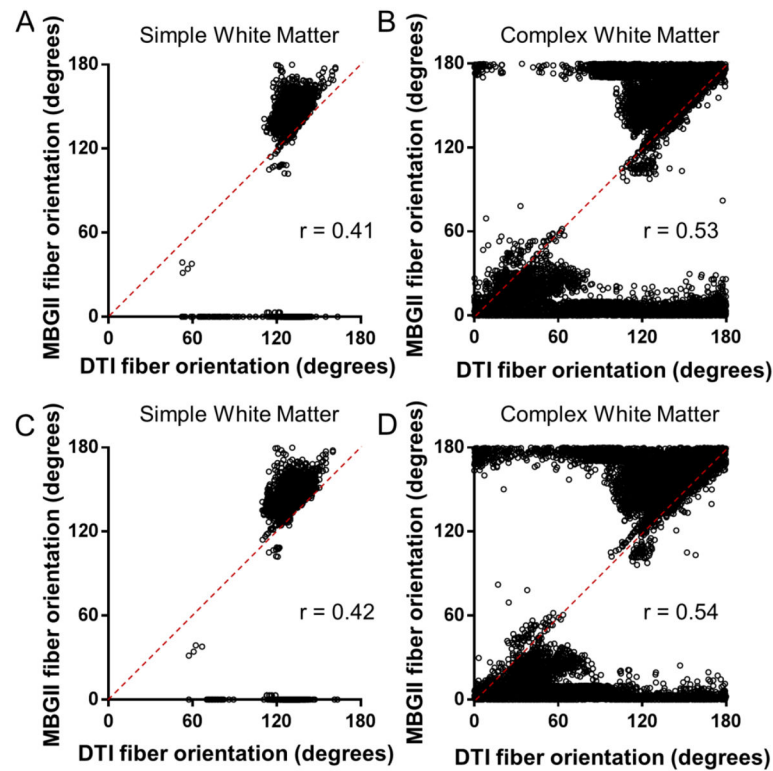
Fig. 10. Fiber direction correlations in a single tensor model
A. DTI derived fiber orientation based on low angular resolution diffusion data (30 directions) vs. Black Gold II derived fiber orientation shows a low correlation (r=0.41) in simple white matter, defined based on GQI data as having only one fiber population. 4.40% of the total voxels in the tissue block were classified as simple white matter. Red line indicates line of identity. **B.** Comparison of DTI and Black Gold II derived fiber orientations in complex white matter, defined based on GQI data as having two fiber populations shows a modest correlation (r=0.53). 22.60% of the total voxels in the tissue block were classified as complex white matter.. **C.** DTI derived fiber orientation based on high angular resolution diffusion data (202 directions) shows a low correlation (r=0.42) with Black Gold II derived fiber orientation in simple white matter. **D.** DTI derived fiber orientation shows a modest (r = 0.54) correlation with Black Gold II derived fiber orientation in complex white matter. The correlations are not affected by using increasing angular resolution, indicating that the single tensor assumption of DTI is not sufficient when modeling voxels with more than one fiber population.
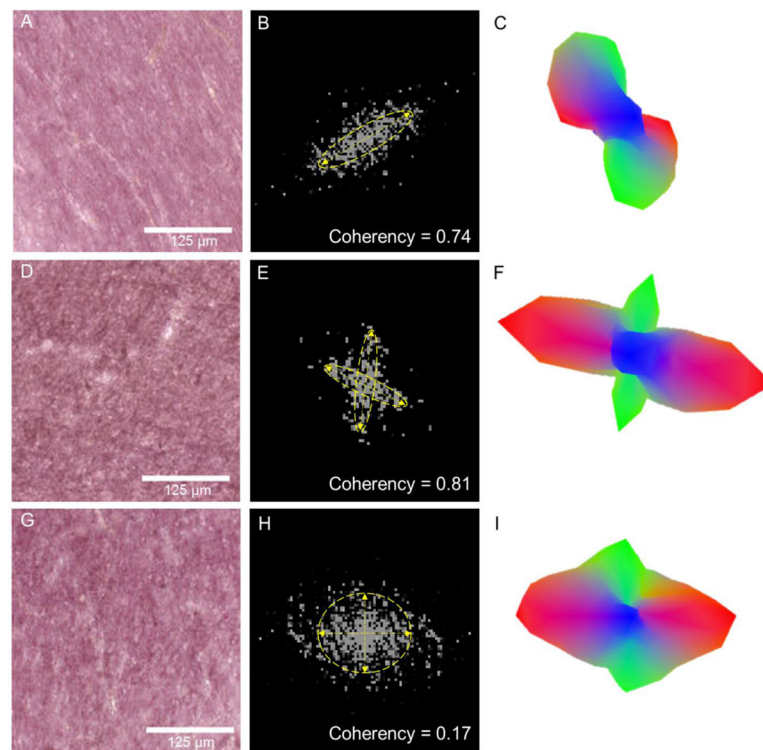
Fig. 11. Power coherence distinguishes between complex vs. disrupted white matter
A. Black Gold II stains myelinated fibers aligned in one orientation. **B.** The power spectrum reflects the strong directional component and coherent fiber architecture (power coherency = 0.74). **C.** The ODF of the coregistered voxel from GQI shows that the white matter fibers in this tract all lie along one direction. **D.** Black Gold II stained examples of crossing fibers. **E.** The power spectrum of these crossing fibers shows two strong directional components, each fitted with two narrow tensors (power coherency = 0.81). **F.** The crossing tracts are apparent in the voxel coregistered to this region, reflected by the two sharp peaks of the function. **G.** Black Gold II stain in a region with disrupted fibers. **H.** The disorganization of the fibers is reflected in the power spectrum, where there is no strong directional component in any direction, resulting in low coherency (power coherency = 0.17). **I.** The ODF from the coregistered voxel reflects the broader spread of directionalities that is observed in the power spectrum of the histological data.
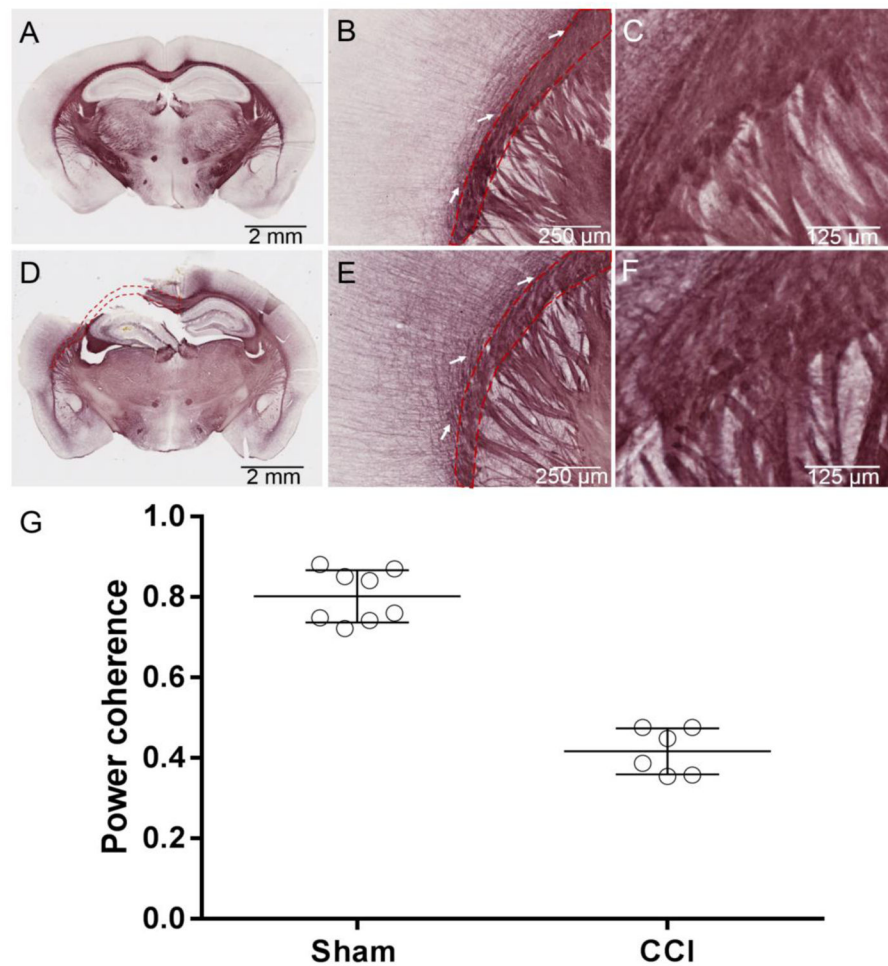
Fig. 12. Power coherence in a mouse model of traumatic brain injury as a positive control
A. 50 μm thick sections from an uninjured mouse brain were stained for myelin using Black Gold II. A region of interest was drawn to include the corpus callosum, restricted to the genu, anterior forceps and external capsule bound by the mideline and the lateral edge of the cingulum on the hemisphere ipsilateral to injury for multiple sections (red line). **B.** Fibers, indicated by white arrows, appear to be curving normally throughout the region. **C.** A high power view of the white matter in the corpus callosum shows that there are no irregularities in fiber organization. **D.** 50 μm thick sections from a positive control (2 mm CCI injury) mouse model of traumatic brain injury were stained for myelin using Black Gold II. A region of interest ipsilateral to the injury site that includes the corpus callosum was drawn for each section (red line). **E.** Fibers, indicated by white arrows, show signs of disruption both in the corpus callosum and as they branch into cortical gray matter. **F.** The high power view of the white matter adjacent to the injury site shows disruption of the underlying fibers. **G.** Power coherence of regions of interest from adjacent sections of both the uninjured and CCI injured mouse was calculated as described in Appendix I. As expected, white matter ipsilateral and close to the injury site in the injured mouse shows signs of disruption, reflected by reduced power coherence. In contrast, white matter in the corresponding region
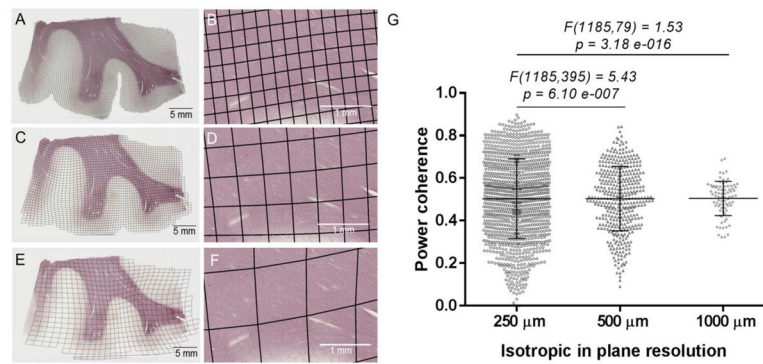
of interest of the uninjured mouse shows consistently high power coherence, reflecting preserved fiber integrity.

Fig. 13. Effect of voxel size on estimations of white matter heterogeneity
A. Voxel-based grids were generated at 250 μm isotropic in plane resolution. **B.** White matter adjacent to sulcal gray matter within a region of interest extending 2 mm into white matter was analyzed for voxel-wise power coherence. **C.** Voxel-based grids were generated at 500 μm isotropic in plane resolution based on landmarks placed on downsampled MRI data. **D.** A 2 mm region of interest of white matter adjacent to sulcal gray matter was analyzed for voxel-wise power coherence. **E.** Voxel based grids were generated at 1000 μm isotropic in plane resolution based on landmarks placed on downsampled MRI data. **F.** The same 2 mm region of interest was analyzed for voxel-wise power coherence. **G.** High in plane spatial resolutions of 250 μm show a large variation in power coherence in white matter adjacent to sulcal gray matter. This region of interest may contain a range of severities of disrupted vs. intact fibers, which should span the range (0–1) of power coherence. As isotropic in plane spatial resolution decreases to 1000 μm, the variation in power coherence is reduced (F = 1.53, p<0.001), indicating that low spatial resolutions may underestimate the heterogeneity of complex white matter regions.

Table 1

Performance of transformation method evaluated using tissue classification

Unweighted kappa coefficients for all ten human cortical tissue samples were calculated for grids generated using the nonlinear vs. affine transformation methods. The kappa coefficient was used to determine the agreement between MRI and Black Gold II histology classified as white matter, gray matter, or boundary tissue on a voxel-wise basis. Nonlinear transformation results in improved tissue classification, reflected by higher kappa coefficients, all higher than 0.90, while the implementation of an affine transformation results in less agreement between MRI and histology based tissue classification, reflected by lower kappa coefficients which are less than 0.90.

Sample #	CTE Stage	Nonlinear transformation		Affine transformation	
		mean κ	± std dev	mean κ	± std dev
Case 1	IV	0.92	0.05	0.78	0.13
Case 2	III	0.94	0.06	0.81	0.22
Case 3	IV	0.91	0.02	0.65	0.17
Case 4	III	0.96	0.08	0.72	0.09
Case 5	IV	0.97	0.08	0.76	0.11
Case 6	III	0.92	0.04	0.67	0.24
Case 7	III	0.93	0.05	0.71	0.23
Case 8	IV	0.94	0.02	0.80	0.19
Case 9	IV	0.95	0.07	0.62	0.08
Case 10	III	0.93	0.03	0.77	0.29